Electronic materials

Stretchable and conductive composites film with efficient electromagnetic interference shielding and absorptivity

Pengdong Feng[1,2,3] , Ziheng Ye[1,2,3] , Qiyuan Wang[1,2,3] , Zheng Chen[4] ,
Guotai Wang[5] , Xiangli Liu[3,*] , Kang Li[1,*] , and Weiwei Zhao[1,2,3,*]

[1] *Flexible Printed Electronics Technology Center, Harbin Institute of Technology, Shenzhen, Shenzhen 518055, People's Republic of China*
[2] *State Key Laboratory of Advanced Welding and Joining, Harbin Institute of Technology, Shenzhen, Shenzhen 518055, People's Republic of China*
[3] *The School of Materials Science and Engineering, Harbin Institute of Technology, Shenzhen, Shenzhen 518055, People's Republic of China*
[4] *China University of Mining and Technology, Xuzhou, People's Republic of China*
[5] *Faculty of Materials and Energy, Guangdong University of Technology, Guangzhou 510006, People's Republic of China*

ABSTRACT

The development of high-performance stretchable and electromagnetic interference (EMI) shielding materials is crucial to the rapidly growing industry of next-generation flexible electronics such as portable electronics and wearable devices. The common approach to EMI shielding is to increase the contents of conductive materials and improve the conductivity. However, this approach is limited by the worse stretchable property. An intrinsically stretchable conductive and EMI shielding thin film (thickness of 0.7 mm) based on functional adhesive (FA) composited by silver nanoparticles (Ag NPs), nickel nanoparticles (Ni NPs), and liquid polydimethylsiloxane (PDMS) is proposed in this paper. The FA is coated onto cured PDMS substrates to fabricate the film, achieving maximum tensile strain of 250% and EMI shielding effectiveness (SE) of 57.1 dB. Up to 35% absorptivity makes an important contribution to SE. This film can withstand more than 20000 stretching-releasing cycles at tensile strain of 0–100% and 0–150%, with no delamination, demonstrating its superior stretchability and repeatability. The mechanism of EMI shielding of silver and nickel nanoparticles is discussed. The durability of these films in terms of electrical and EMI SE properties are also tested. In addition, a device to change the output power of a transformer is constructed.

Pengdong Feng and Ziheng Ye have contributed equally to this work.

Address correspondence to E-mail: xiangliliu@hit.edu.cn; likanghit2004@163.com; wzhao@hit.edu.cn

Introduction

Stretchable devices have developed well in the fields of wearable electronics and advanced medical devices, such as non-planar ports of communication electronics and stretchable artificial organ scaffolds in biomedical applications. Bottlenecks in the study of stretchable devices have emerged, one of which is how to shield the electromagnetic interference (EMI). EMI to communications, electronic equipment, medical equipment, and humans themselves can cause reduced signal-to-noise ratio (SNR), chip failure, cardiac pacemaker arrest, and even abortions in pregnant women. Such serious consequences have stimulated much interest into the research of the stretchable and EMI shielding devices.

Electromagnetic interference shielding can be carried out by utilizing the ultra-high conductivity of silver nanowires (Ag NWs) [1], silver nanoparticles (Ag NPs), and silver coated copper powders [2], which are composited or connected to poly(ethylene terephthalate) (PET) [3] or polyimide foam [4] substrate. With the magnetic properties of iron, cobalt, and nickel, Fe–Ni laminated composites, Ni–Co–P composites, carbon nanotubes, carbon fibers with Ni–Fe_3O_4, and Co/Ni–CNTs all exhibit high shielding effectiveness (SE) at X band (8–12 GHz) [5–9]. According to Schelkunoff electromagnetic shielding theory, this is due to introduced permeability. However, these materials above are neither flexible nor stretchable. Non-stretchable shielding materials, including graphene oxide (GO) film [10], reduced GO-WPU composites [11], PES/Ag NWs/PET [12], Pd-CNT-Cu bucky paper sandwich structure [13], Au/multi walled CNT (MWCNT)-PVDF composites [14], polymer/MWCNT [15], reduced GO/Fe_3O_4 [16], graphite [17], 2D transition-metal carbide thin films [18], and G-CNT-Fe2O3 multilayers [19] are studied, producing SE of 38–134 dB. Meanwhile, stretchable conductors such as Ag-doped graphene fiber [20], Cu–Ag core–shell nanowire/elastomer [21], CNT/eco-flex [22], reduced GO [23], G-metal nanowire [24] do not contain EMI shielding properties.

Present research on stretchable and EMI shielding materials is detailed as follows. Liquid metallic split ring resonators (SRRs) embedded in eco-flex have been shown to only display the peak SE at specific frequencies [25]. Single-walled CNTs (SGCNTs) [26]

were blended into fluorinated rubber, and prominent stretchable property was obtained with the SE of 22 dB. A quartz fiber cloth-reinforced MWCNTs carbon aerogel and PDMS was found to display the SE of 20 dB and 45% stretchable property [27]. Rubber composites of Ag NPs/SBS required the weight fraction of Ag NPs to be greater than 55%, but displayed strain of less than 60% [28]. Acceptable SE was achieved using Ag NWs percolation network in PDMS with a tensile strain of 50% [29]. Another study blended PEDOT/PSS with stretchable WPU, which exhibited an adequate SE of 62 dB, but an elongation of 32.5% [30]. Using a dipping-drying method, Cu- and Ag-coated fabrics reached a strain of 100% with poor SE [31]. Butyl rubber [32] has also been investigated, and was mixed with SGCNT by solution processing to withstand strain of 1000%; however, the SE only reached 13 dB at X band. Although the robustly super-hydrophobic conductive textile composited with Ag NWs, CNTs can shield EMI; large pre-strained textile is need to achieve stretchability [33].

Electromagnetic wave reflection at heterogeneous interfaces (gas–solid and solid–solid interface) is an effective method to improve the absorptivity of EMI, which leads to a substantial increase of SE [34, 35]. Interfacial reflection causes more wave crests and troughs to coincide and superimpose, resulting in a total amplitude of zero and heat dissipation [36]. Thus they can be used in the next generation of wearable electronic pressure sensors [37], photodetectors [38] and human health monitors [39]. For composite materials, increasing the content of the non-stretchable conductive materials will correspondingly reduce the polymer matrix content, which will inevitably deteriorate the flexibility and stretchable property of the devices. Also, the upper limit of the conductive materials content in the composites limits the further improvement in conductivity. In evaluating the research thus far, it is clear that the method improving the SE of EMI shielding materials without compromising the stretchable property is to introduce more heterogeneous interfaces.

In this paper, a prominent stretchable conductive and EMI shielding film with functional adhesive (FA) layers is discussed. Functional adhesive composited by Ag NPs with high conductivity, Ni nanoparticles (Ni NPs) with capable magnetism, and liquid PDMS are coated onto a cured PDMS substrate, obtaining a

film with laminated structure. The mechanism of shielding EMI of Ag NPs is different from that of Ni NPs. Unlike the increase in conductivity alone, adding magnetic Ni NPs can further improve the SE despite a slight decrease in conductivity due to the reduction in the content of Ag NPs. The structure of FA layers, type, and content of electrically conductive components in FA are three major factors determining the EMI SE of the film. When the conductive components in FA are Ag NPs [FA(Ag)], Ni NPs [FA(Ni)], and both combined [FA(Ag + Ni)], the films exhibit diverse conductive and EMI shielding properties. The best performance was achieved by FA(Ag + Ni) − 1(M(Ag) = 35% and M(Ni) = 14.8%), which displayed the repeatable stretchable property (up to 225%), and the EMI SE as high as 57.1 dB. The effect of Ag NPs and Ni NPs on enhancing the absorptivity and reflectivity of EMI is also studied. The films can withstand more than 20000 stretching-releasing cycles at tensile strain of 0–100% and 0–150%. Excellent durability is also demonstrated by testing the electrical properties and EMI SE of such films after 10 days. Additionally, a device that interferes with the transmission of electromagnetic signals is constructed.

Experimental section

Preparation of Ni nanoparticle

The chemical equation is given by:

$$2NiCl_2 + N_2H_4 + 4NaOH = 2Ni\ (solid) + N_2\ (gas) \\ + 4H_2O + 4NaCl$$
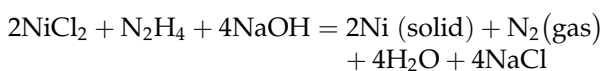
Four types of solutions are initial prepared as reactants: $c(NaOH) = 11$ mol/L, $c(NiCl_2 \cdot 6H_2O) = 1.5$ mol/L, $c(N_2H_4) = 3$ mol/L, and $c(PVP) = 0.32$ g/mL, and the solvent is deionized water. Among the solutions, PVP (polyvinylpyrrolidone, K29-32) is used as a dispersant and does not participate in the reaction process. Following this, 1 mL of PVP solution is added to 10 mL of NiCl2 solution, followed by 3 mL of NaOH solution. After magnetic stirring for 30 min, 5 mL of hydrazine hydrate (N_2H_4) solution is slowly added into the mint green solution and magnetic stirring continues for 30 min. The solution obtained by the above reaction is poured into a reaction vessel, which is then placed in a vacuum oven and kept at 130 °C for 4 h. Following this process, the reaction vessel is placed in water and

cooled to room temperature. Thereafter, the product in the vessel and absolute ethanol are both poured into a close tube, which is centrifuged at 4000 r/min for 5 min, and this separation is repeated three times. Absolute ethanol is used to remove residual PVP from the sediment. Finally, the sediment is dried in an oven at 50 °C for 30 min, and nickel nanoparticles are obtained.

Preparation of Ag nanoparticle

Silver particles are prepared by a method of reducing silver ions using a strong reducing agent. To reduce particle size, PVP is used as a dispersant. The specific process is as follows. Silver nitrate ($AgNO_3$) is added to 180 mL deionized water at a silver ions (Ag^+) concentration of 0.0055 mol/L, followed by adding polyvinylpyrrolidone (PVP) to $AgNO_3$ solution as dispersant. The weight ratio of $AgNO_3$ to PVP is 1:1. After magnetic stirring, a transparent solution with no color is obtained. Next, 5 mL hydrazine (Macklin, 50%) is slowly dropped into the above solution, and a redox reaction occurs. After mechanical agitation for about 90 min, the chemical reaction is completed and a black precipitate is obtained. The precipitated material at this time consists of PVP-coated silver nanoparticles (Ag NPs) and residual liquid. The PVP coating and residual liquid are then removed by ultrasonic cleaning with absolute ethanol. The liquid and solids in the washed mixture are separated by centrifugation (4000 r/min, 5 min). After the washing and centrifugation process, a mixture of silver nanoparticles with a very thin PVP coating layer and residual absolute ethanol is obtained. The mixture is then dried at 50 °C for 60 min to produce a pure solid. Finally, gray-black silver nanoparticles are obtained by grinding and sifting.

PDMS substrate preparation

The PDMS substrate is made from polydimethylsiloxane by mixing the base monomer and a curing agent at 10:1 (w:w) (Sylgard 184, Dow Corning). This liquid PDMS is poured into a prefabricated template (the thickness of the rectangle substrate–film is 0.5–0.8 mm) and left in the air for 1 h to remove air voids. Next, the PDMS substrate and template are thermally cured in an electric thermostat blast drying chamber at suitable temperature (50 °C) and dwell time (112 min), then PDMS substrates are peeled off the template. The two parameters, temperature and

dwell time, are not independent of each other. Dwell time increases as temperature decreases.

Functional adhesives synthesis

The prepared Ag NPs, Ni NPs, and liquid PDMS are uniformly mixed by mechanical stirring and ultrasonic dispersion.

Fabrication of stretchable conductive shielding film

Fluid FAs are coated onto the PDMS substrate, and the FA layer is kept flat. After sintering at a low temperature (50 °C) for a short period of time in the oven (20 min), the film is obtained.

Characterization

Current vs voltage curves were obtained by electrochemical workstation (Nova Auto-lab), with applied voltage speed of 0.05 V/s, and range of 0–1 V. XRD maps were analyzed by X-ray diffraction analyser, with current of 40 mA, voltage of 200 kV, speed of 5°/min, and range of 10°–80°. Magnetic hysteresis loop was measured by VSM, where the sample shape was a annulated concrete column (inner diameter 14 mm, outer diameter 20 mm, height 2 mm). SEM images and EDX maps were analyzed by field emission scan electron microscope, with voltage of 15 kV and scanning backscattered electrons. Films were fixed on the leadscrew rail to withstand stretching-releasing cycles. EMI SE was tested by vector network analyser, with rectangle sample size of 33×33 mm^2. To ensure that the entire test area is occupied, the sample size is larger than required (22.86×10.16 mm^2). The particle size was measured by Malvine nanoparticle size and ZETA analyzer, which were applied 11 transmission cycles to the turbid liquid of nanoparticles.

EMI shielding effectiveness test

For a two-port network in a radio frequency signal, there are two scattering parameters $S11$ and $S21$. $S11$ is the reflection coefficient and input standing wave of port 1 when port 2 matches, which describe the matching of input end of device. $S21$ is the gain or insertion loss in radio frequency networks, which describes the magnification or attenuation of a signal

passing through a device. A square film (33 * 33 mm^2) is fixed on the jig of vector network analyzer (Keysight, E5063A). Frequency range is set as 8–12 GHz. Then $S21$ (dB) and $S11$ (dB) are recorded to convert into EMI SE, and the percentage of reflectivity, absorptivity, and transmissivity given by:

$$S21(mW) = 10^{S21(\text{dB})/20} \tag{1}$$

$$S11(mW) = 10^{S11(\text{dB})/20} \tag{2}$$

$$E_t = S21(mW) \times S21(mW) \times 100\% \tag{3}$$

$$E_r = S11(mW) \times S11(mW) \times 100\% \tag{4}$$

$$E_a = 1 - E_t - E_r \tag{5}$$

$$\text{EMI SE(dB)} = 10 \times \log_{10}(1/E_t) \tag{6}$$

where E_t, E_r and E_a is the percentage of transmissivity, reflectivity, absorptivity, respectively.

Results and discussion

Fabrication and characterization of the films

The fabrication process of the FA/PDMS film is provided in Fig. 1a. First, electrically conductive nanoparticles and solid PDMS substrates are prepared in laboratory. Considering the electrical conductivity and stable dispersion of the composite, the key points in the preparation of the conductive functional adhesives herein are that no large-area agglomeration occurs and most of the gaps are less than 10 nm [40]. The preparation process of Ag NPs, Ni NPs and FA is described in the above experimental section. The prepared Ag NPs, Ni NPs and liquid PDMS are then uniformly mixed by mechanical stirring and ultrasonic dispersion, followed by coating the FA onto solid PDMS substrates. Thickness of FA layers is designed to be 0.7 mm. After 12 h, a stretchable shielding film with a strong interface between FA layer and substrates is obtained due to both materials containing the same polymer (PDMS). Here the ratio of Ag NPs and Ni NPs should be determined. When solid particles are mixed with fluid, the mass fraction of the particles has an upper limit, which is define here as M$_{\text{lim}}$. At this point in the process, the mixture is barely considered a fluid. In order to take advantage of the stretchable property of PDMS, the condition of M(Ag) < M$_{\text{lim}}$ (Ag) in FA is required. However, optimizing the current percolation of materials is one of the main methods to
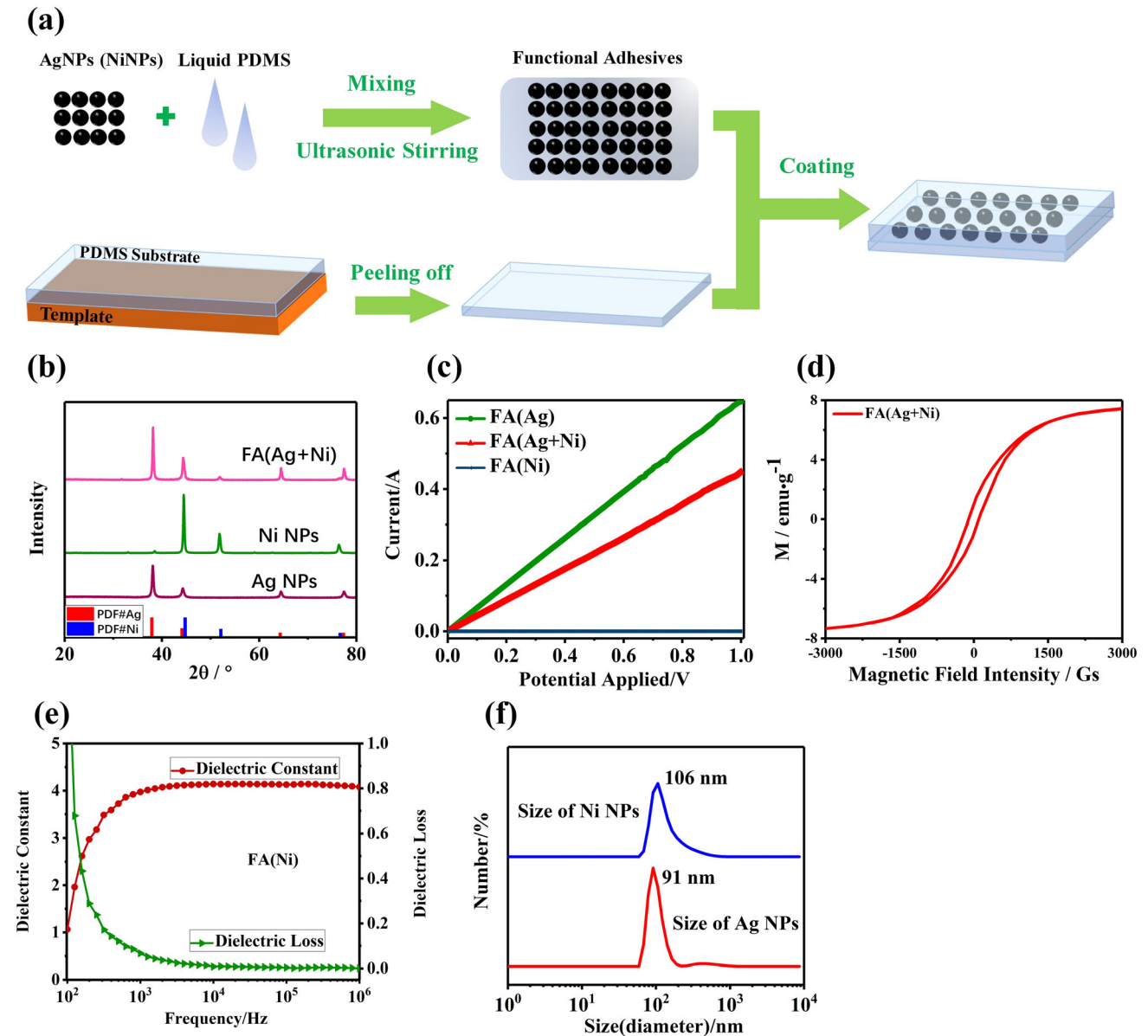
Figure 1 **a** Fabrication process of the FA/PDMS film; **b** XRD analysis on the conductive fillers and FA; **c** Current versus voltage curves of FA(Ag), FA(Ag + Ni), and FA(Ni); **d** magnetic hysteresis loop of FA(Ag + Ni); **e** dielectric performance of FA(Ni) with W(Ni) = 57%; **f** particle size distribution of the prepared Ag NPs and Ni NPs.

improve the effectiveness of shielding, which limits the lowest amount of Ag NPs, M_{lowest} (Ag). As a result, the contents of Ag NPs in FA are required to meet the condition of M_{lim} (Ag) > M(Ag) > M_{lowest} (Ag). Similarly, the condition of M_{lim} (Ag + Ni) > M(Ag) + M(Ni) > M_{lowest} (Ag + Ni) should also been met. An X-ray diffraction (XRD) analysis of Ag NPs, Ni NPs, and FA(Ag + Ni) is provided in Fig. 1b. The mass content of silver and nickel in FA(Ag + Ni) is M(Ag) = 33%, and M(Ni) = 14.8%, respectively. The diffraction peaks of

FA are the superposition of peaks of silver and nickel. A weak peak at $2\theta = 38.48°$ appeared in the prepared Ni NPs, which represents residual oxides of carbon or sodium. The current vs voltage curves of FA (Ag), FA (Ag + Ni), and FA (Ni) are illustrated in Fig. 1c. As the conductive mechanism is electrical current percolation [41], the C–V curves are almost straight lines with constant slopes. Electrical conductivity of FA (Ag) is higher than that of FA (Ag + Ni), while FA(Ni) is close to being an insulator of electricity. Magnetic hysteresis loop of FA (Ag + Ni) is given in

Fig. 1d, and the coercive force (Hc) is − 113 Gs. The saturation magnetization (Ms) is 7.4 emu g^{-1} when the applied field intensity reaches to 3000 Gs. The dielectric properties of FA(Ni) are given in Fig. 1e. The mixed Ni NPs could enhance the polarization of polymers, and thus, the dielectric constant is improved to 4.14 while the dielectric loss is less than 0.01. The particle size, shape of nanoparticles, and related dispersion state in the polymer play an important role in the properties of composite polymers. Figure 1f shows that particle sizes of Ag NPs and Ni NPs are mainly located near 91 nm and 106 nm, respectively. The sizes are measured by Malvine ZETA analyzer. Eleven transmission cycles are applied to the turbid liquid of nanoparticles to ensure the data accuracy. The FA/PDMS film in this paper exhibits EMI SE of 57 dB and can withstand tensile strain of up to 250%, the details of which are explained in the context of the conditions outlined in the following sections.

SEM images and dispersion states

Figure 2 shows the filed-emission scanning electrons microscopic images. The spherical Ag NPs prepared in this study are shown in Fig. 2a. The morphology of Ni is a micron-sized irregular group composed of several Ni NPs, which is demonstrated by Figs. 1f and 2b. These micron-sized Ni groups are uniformly distributed in the PDMS matrix, and the gaps between them are much larger than 100 nm, shown in Fig. 2c. Percolation and tunneling could not occur, and thus, the FA(Ni) is dielectric composites. Cross-sectional image (Fig. 2d) of FA(Ni) exhibits the existence of porosity, which is caused by the oxides in the prepared Ni NPs. Dispersion states of Ag NPs in the FA(Ag) are shown in Fig. 2e. The dark regions are PDMS matrix, which have fully filled all the gaps between every Ag NP. The surface and edges of the Ag NPs cannot be clearly photographed due to the covering of organic matter. Figure 2f and g is the same one image of FA(Ag), which are used to the comparative analysis of particle spacing. Five silver nanoparticles are marked by red circles and numbered from 1 to 5. The spaces between particle 1 and 2, and between 3 and 4, are all less than 10 nm, which results many electrons hopping and appear the percolation. Although the space between particle 4 and 5 is larger than 10 nm, the three-dimensional stacks of Ag NPs can percolate over a large area to improve the conductivity of FA(Ag). Figure 2h and i is the same one image to show the dispersion states of Ag and Ni in the FA(Ag + Ni). The interfaces are located between Ag NPs and Ni NPs. The Ni NPs cause various porosities in FA(Ag + Ni), which are displayed in the cross-sectional images in Fig. 2j and k. The energy-dispersive X-ray spectrometry (EDS) maps of FA(Ag + Ni) are illustrated in Fig. 2l. Here it can be seen that the Ag NPs and Ni NPs are distributed across most of the area, while PDMS occupies almost all gaps between nanoparticles. Applied strain is coordinated by PDMS and percolation current is transmitted by nanoparticles. The Ni NP contributes less to percolation due to these large spacing, leading to the poor conductive properties of FA(Ag + Ni). Figure 2m provides the EDS maps of FA(Ag). The Ag NPs are uniformly distributed within this area, and PDMS, represented by silicon, exists in the gaps.

Electrical and mechanical properties

The electrical and stretchable properties are illustrated in Fig. 3. The electrical resistance at different strain is shown in Fig. 3a. The inset is the schematic structure of the sample with FA(Ag) layer and M(Ag) = 42%. The layer are joined onto the PDMS substrate. Maximum tensile strain while remaining conductive is 250%, and sheet resistance at strain of 250% is only 1.43 Ω sq^{-1}. For the FA(Ag), the sheet resistance value during the stretching–releasing–re-stretching cycles at tensile strain of 0–100% and 0–150% is shown in Fig. 3b. The insets in Fig. 3b are ε-time curves. These insets curves show the changes of strain of the sample in two stretching-releasing cycles. The strain of the sample is marked by ε. The more cycles, the more time. For each cycle, the strain of the samples increases from 0 to 100% (150%) and then decreases from 100 (150%) to 0%. The data points of all curves in Fig. 3b are the resistance of the sample at strain of 0% after enduring the corresponding number of cycles. As shown in Fig. 3b, the resistance of FA(Ag) increased from 0.230 to 1.546 Ω/sq, after the sample withstanding 10000 stretching–releasing cycles of 0–100–0%. Thereafter, the film continues to withstand stretching-releasing cycles at strain of 0–150–0%, leading to an increase in sheet resistance by 769% after 5000 cycles, and growing to 13.48 Ω sq^{-1} after 10000 cycles.
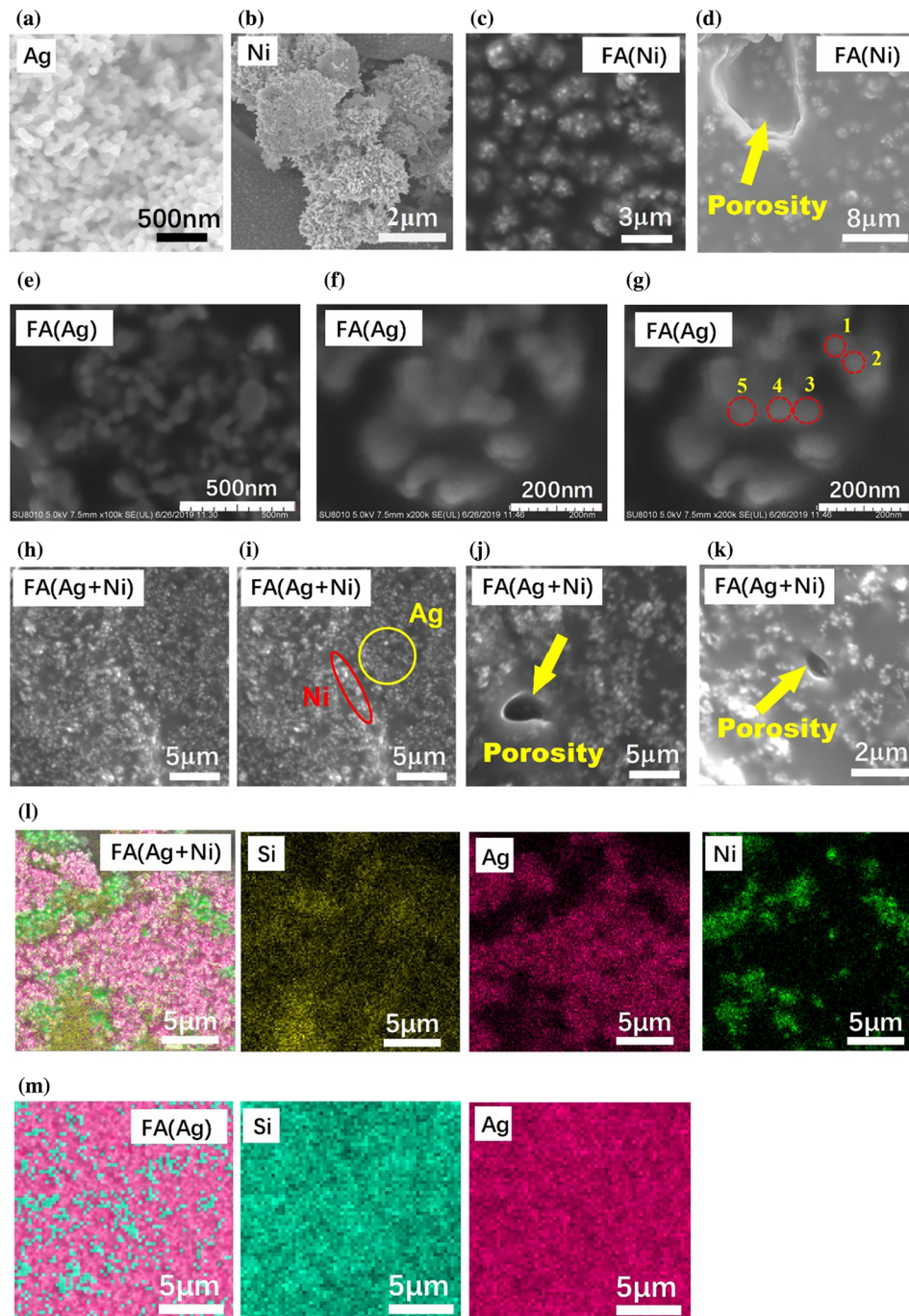
Figure 2 SEM images of all the materials used in this study. **a** Ag NPs, **b** Ni NPs, **c** dispersion state of Ni in the FA(Ni) and **d** cross-sectional image and the porosity in the FA(Ni). **e–g** Dispersion states of Ag NPs in the FA(Ag), **f** and **g** are the same one image, **g** illustration of the distances between the nanoparticle edges.

h and **i** are the same one image to show the dispersion states of Ag and Ni in the FA(Ag + Ni). **j** and **k** are the cross-sectional images and the porosities in the FA(Ag + Ni). **l** EDS maps of the Si, Ag, Ni elements in the FA(Ag + Ni). **m** EDS maps of the Si, Ag elements in the FA(Ag).

The film consisting of a sandwich structure is illustrated in the inset of Fig. 3c. The top layer is FA(Ni) and M(Ni) = 57%, and the middle layer is FA(Ag) and M(Ag) = 42%. The thickness is the same as the previous sandwich structure. The sheet resistance value during the stretching–releasing–re-
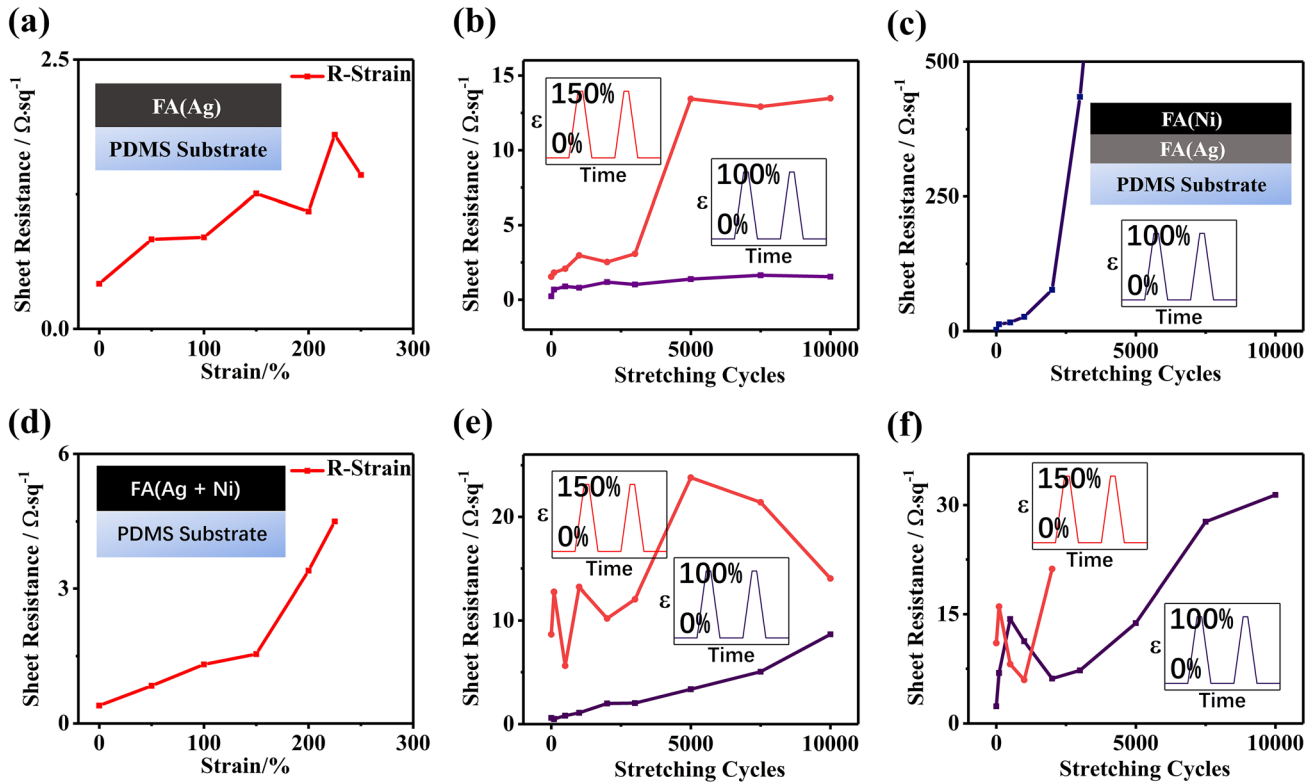
Figure 3 Stretchable properties of these samples. For films with FA(Ag) layer: **a** sheet resistance at different tensile strain (up to 250%), insets show the structure schematic of this film. **b** Sheet resistance under stretching–releasing cycles at tensile strain of 0–100–0% and 0–150–0%, two insets (ε-time curves) show the strain of corresponding samples in each cycle. For films with sandwich structure: **c** Sheet resistance under stretching–releasing cycles, inset diagrams are ε-time curves, and inset schematic shows the structure of this film. For the FA(Ag + Ni) − 1, the two properties are illustrated as follows: **d** Sheet resistance at different tensile strain, inset shows the structure schematic of this film with FA layer thickness of 0.7 mm, **e** sheet resistance under stretching-releasing cycles, two insets are ε-time curves. For the FA(Ag + Ni) − 2, the mechanical properties are illustrated as follows: **f** Sheet resistance under stretching-releasing cycles, two insets are ε-time curves.

stretching cycles at tensile strain of 0–100–0% is shown in Fig. 3c. The inset diagram (ε-time curves) shows the strain of corresponding samples in each cycle. Its initial value is only 1.957 Ω sq^{-1}, which sharply increases to 435 Ω sq^{-1} after 3000 cycles at strain of 0–100%. Thereafter, this film struggles to maintain conductivity after 5000 stretching–releasing cycles.

Combining the two mechanism of Ag NPs and Ni NPs, FA(Ag + Ni) of various mass ratio is fabricated. This material demonstrates higher EMI SE and excellent conductivity and stretchable property. When M(Ag) = 35% and M(Ni) = 14.8%, the sample is marked by FA(Ag + Ni) − 1, and maximum tensile strain while remaining conductive is 225%, and sheet resistance at strain of 225% is less than 4.5 Ω sq^{-1}, as shown in Fig. 3d. The inset is a schematic of the structure of this film, and the thickness of the layer and substrate is designed to be 0.7 mm and 0.5 mm, respectively. For the FA(Ag + Ni) − 1, the sheet resistance value during the stretching–releasing–re-stretching cycles at tensile strain of 0–100–0% and 0–150–0% is shown in Fig. 3e. The inset diagrams (ε-time curves) show the strain of corresponding samples in each cycle. Its initial value is only 0.574 Ω sq^{-1}, which steadily increases to 8.66 Ω sq^{-1} after 10000 cycles at strain of 0–100–0%. Thereafter, this film continues to withstand 10000 stretching-releasing cycles at strain of 0–150–0%, leading to fluctuations of sheet resistance in the range of 5.62–21.41 Ω sq^{-1}. When M(Ag) = 33% and M(Ni) = 14.8%, the sample is marked by FA(Ag + Ni) − 2. Figure 3e illustrates the sheet resistance value during the stretching–releasing–re-stretching cycles at tensile strain of 0–100–0% and 0–150–0%, when M(Ag) = 33% and M(Ni) = 14.8%. The inset diagrams (ε-time

curves) show the strain of corresponding samples in each cycle. The inset in Fig. 3e is a schematic of the structure of this film. Its initial value is only 2.32 Ω sq^{-1}, which rapidly increases to 30 Ω sq^{-1} after 10000 cycles at strain of 0–100–0%. One day later, this film continues to withstand 2000 stretching–releasing cycles at strain of 0–150–0%, leading to fluctuations of sheet resistance in the range of 11–21 Ω sq^{-1}, before failure occurs.

The EMI shielding performances

The EMI shielding properties of these samples are shown in Fig. 4. The shielding efficiency (SE) of the above 4 samples are given in Fig. 4a. The FA(Ni) layer has been studied specifically.

For the FA(Ag), the EMI SE of this film at frequency range of 8–12 GHz is relatively high at 43.6–52.8 dB. After passing through the film, the energy of the electromagnetic wave exists in three aspects: reflection (E_r), absorption (E_a), and transmission (E_t). Percentages of the three parts are provided in Fig. 4b. The transmissivity is less than 0.0045%, so its curve is placed in the bottom of this coordinate system. Reflectivity is 50.4–61.7%, which is larger than the absorptivity of 38.2–51.5%. The higher frequency, the lower the reflectivity, but higher the absorptivity.
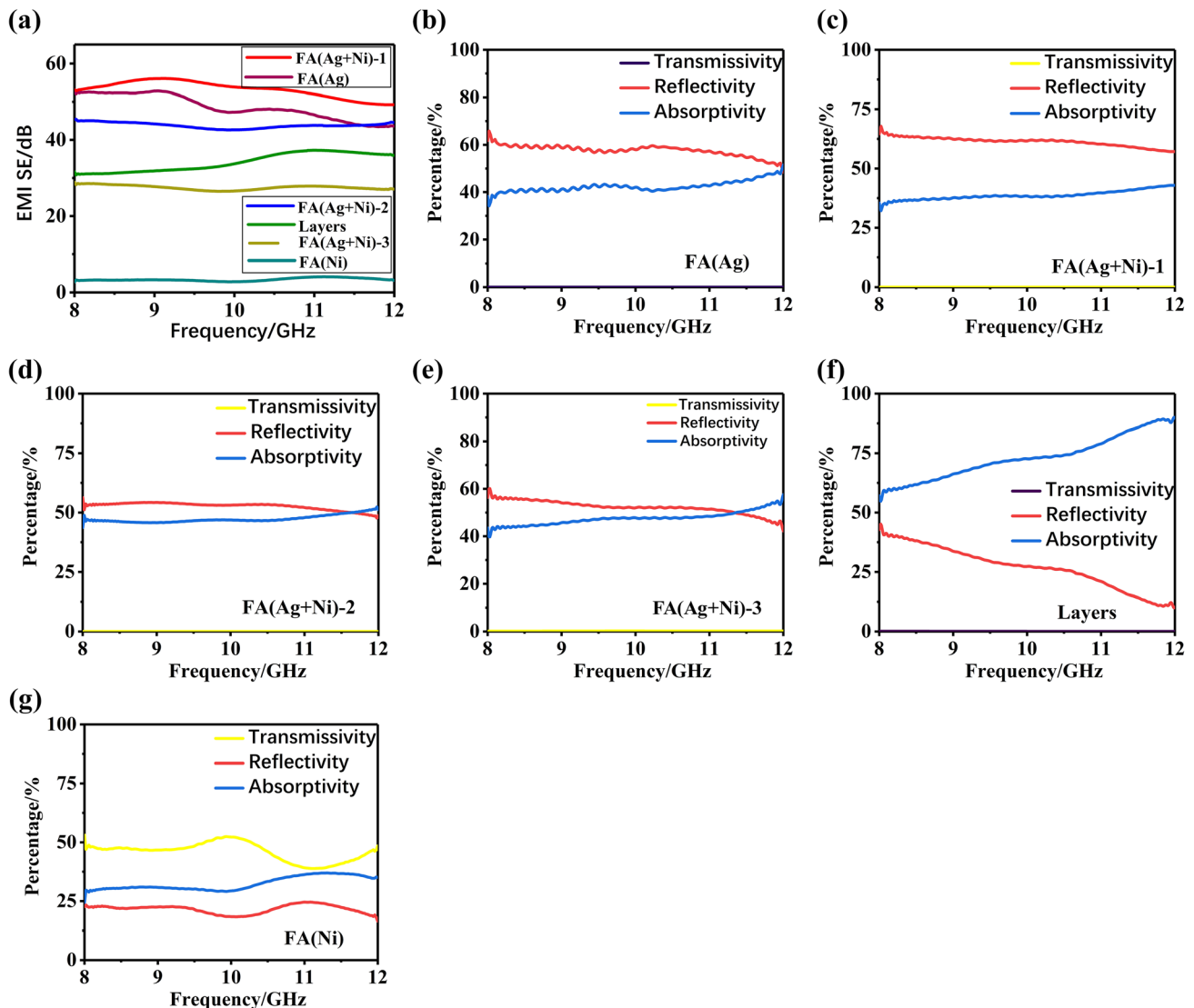

Figure 4 The shielding properties of these samples. **a** EMI SE of these samples at X band. The percentage of E_r, E_a, E_t for the **b** FA(Ag), **c** FA(Ag + Ni) − 1, **d** FA(Ag + Ni) − 2, **e** FA(Ag + Ni) − 3, **f** Layered FA, and **g** FA(Ni).

For the FA(Ag + Ni) − 1, the EMI SE at frequency range of 8–12 GHz is elevated to 57.1 dB. This value is slightly higher than the SE of the film with an FA(Ag) monolayer, exhibiting the advantage of introducing Ni NPs. Percentages of the E_r, E_a and E_t are provided in Fig. 4c. Transmissivity is as low as 0.00024%, so the curve is also placed in the bottom of the coordinate system. Reflectivity is 57.0–65.2%, obviously larger than absorptivity of 35.3–43.0%. The higher the frequency, the lower reflectivity, but higher absorptivity.

For the FA(Ag + Ni) − 2, the EMI SE of this film at frequency range of 8–12 GHz is approximately 44 dB. The value is 22% lower than the SE of FA(Ag + Ni) − 1. Percentages of the E_r, E_a, and E_t are provided in Fig. 4d. Transmissivity is as low as 0.00292%, so its curve also places in the bottom of the coordinate system. Reflectivity is 52%, which is slightly larger than absorptivity of 48%. These two curves are very close, and absorptivity is even larger than reflectivity in the range of 11.6–12 GHz.

In addition, a third proportion (M(Ag) = 33.4% and M(Ni) = 14.5%) was studied, and its sample was marked by the FA(Ag + Ni) − 3. After reducing the nickel content, the EMI SE of this film at frequency range of 8–12 GHz is only 28 dB (Fig. 4a). The value is 50% lower than the SE of FA(Ag + Ni) − 1. Percentages of the E_r, E_a, and E_t are provided in Fig. 4e. Transmissivity is 0.129% at 8 GHz. Reflectivity is 56%, which is slightly larger than absorptivity of 43%. The absorption ratio was also reduced by the decrease in nickel content and the change in the mass ratio of silver to nickel.

For the three-layers sample (the sandwich structure), the EMI SE of the film at frequency range of 8–12 GHz is about 30.9–37.3 dB. Percentages of the three parts, E_r, E_a, E_t, are given in Fig. 4f. Transmissivity is less than 0.08%, so the curve is placed at the bottom of the coordinate system. Absorptivity is 57.2–90.0%, much larger than reflectivity of 9.9–42.7%. The SE here is lower than the value of FA(Ag) monolayer. Therefore, the multilayer structure in which silver and nickel are distributed in different layers cannot be used as an excellent stretchable and EMI shielding film.

For the FA(Ni) (not sandwich structure), the layer is joined with a PDMS substrate, and its structure size is similar to the FA(Ag) sample. No electrical properties of this sample made up of FA(Ni) and M(Ni) = 57% are tested due to no occurrence of percolation. The EMI SE of this film at frequency range of 8–12 GHz is reasonably low at 3.1–4.1 dB. The percentages of the three parts, E_r, E_a, E_t are provided in Fig. 4g. Transmissivity is 38.8–53.1%, demonstrating that around half of the electromagnetic energy can pass through this film. However, across the entire range of 8–12 GHz, absorptivity is obviously larger than reflectivity, indicating that the mechanism of shielding EMI of Ni NPs is different from that of Ag NPs. So introducing Ni NPs into FA(Ag) may further improve the SE without loss of stretchable properties.

Durability results of FA(Ag) and FA(Ag + Ni)

Durability testing is conducted, as the long-term stability of the film function is a necessary condition for the practical application of flexible electronics. For the FA(Ag + Ni) − 1 (M(Ag) = 35% and M(Ni) = 14.8%) layers, the sheet resistance value changes with time, as shown in Fig. 5a. Although there are small fluctuations, the resistance remains below 0.398 Ω sq^{-1}, indicating the excellent electrical property stability of FA(Ag + Ni). The EMI SE of the same film after 1 and 15 days is provided in Fig. 5b. The two curves are almost intertwined, indicating that the shielding efficiency remains at 49.2–57.1 dB. Percentages of the E_r, E_a and E_t after 15 days are shown in Fig. 5c, which are not much different from the initial state. Transmissivity is less than 0.0008%. Reflectivity is 52.2–63.0%, larger than absorptivity of 36.98–47.8%.

When M(Ag) = 42% for FA(Ag) layers, the sheet resistance value changes with time, as shown in Fig. 5d. The initial sheet resistance is 0.137 Ω sq^{-1} and remains below 0.309 Ω sq^{-1} within 30 days, indicating the superior electrical property of FA(Ag) compared to FA(Ag + Ni). The durability of EMI SE for the same film after 15 days is provided in Fig. 5e. The two curves are also intertwined, indicating that the shielding efficiency remains at 43.6–52.8 dB, without obvious fluctuation; however, its SE is lower than the layer of FA(Ag + Ni). Percentages of the Er, Ea, and Et after 15 days are given in Fig. 5f. Transmissivity is less than 0.003%, and reflectivity is 48.7–56.9%, slightly larger than absorptivity of 43.1–51.3%.
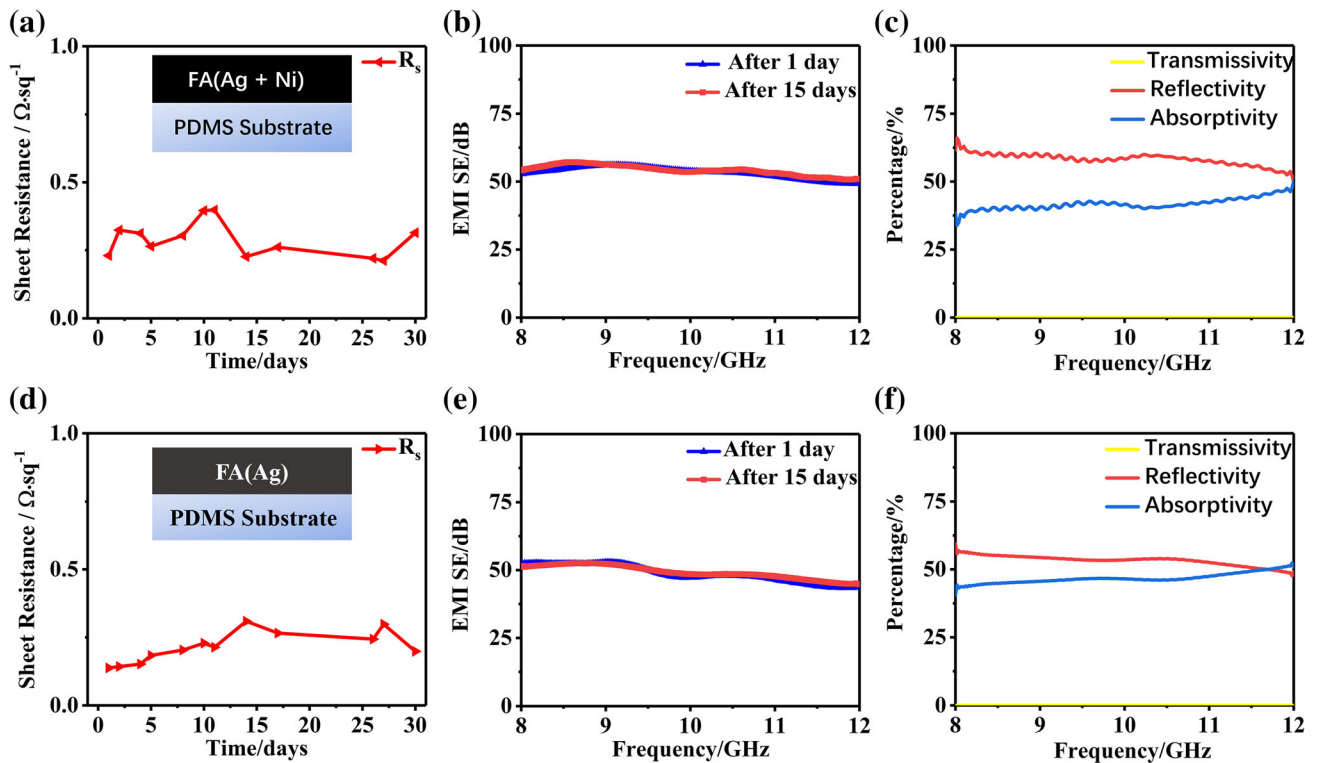
Figure 5 Durability test results. For FA(Ag + Ni): **a** Sheet resistance change within 30 days; **b** EMI SE after 1 and 15 days; **c** percentage of E_r, E_a, E_t after 15 days. For FA(Ag): the above three properties are shown in **d**–**f**, respectively. Insets in **a** and **d** are the structure of these films.

Horizontal comparison with similar results by other groups

Here, in order to emphasize the prominent result, we have summarized the results of the existing stretchable and EMI shielding materials, and the results are shown in Fig. 6. In this work, the performance of FA(Ag + Ni) − 1 is represented by the red five-pointed star. The other seven works have been cited in the References section, and their performances are represented by the other seven icons in Fig. 6. It is shown that the EMI SE and stretchability have been simultaneously improved in this work.

Discussion

The mechanism of the high SE is worthy to be investigated, of which the schematic is shown in Fig. 7. As the percentages of absorptivity are much larger than 10%, the dissipation of EMI occurred inside the FA have been studied.

As shown in Fig. 7, the Ag NPs in FA forms conductive networks in which a large amounts of hopping and migrating electrons dissipates the energy of the incident electromagnetic wave. As a result, contents of silver nanoparticles in FA(Ag) are limited in the range of 40–42%, and thus, the EMI SE of a film with FA(Ag) layer can exceed 50 dB.

Although no percolation appears, FA(Ni) monolayer exhibited shielding performance. When an electromagnetic field (EMI) is applied, these magnetic particles are magnetized and induce an obstructed magnetic field. Also, FA(Ni) become polarized and
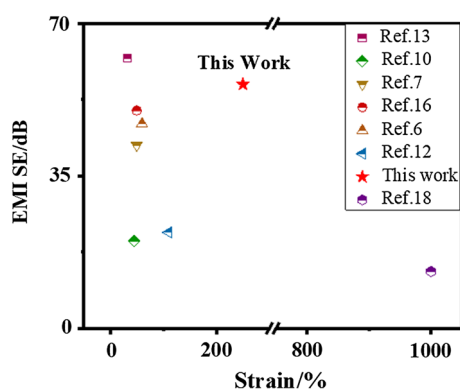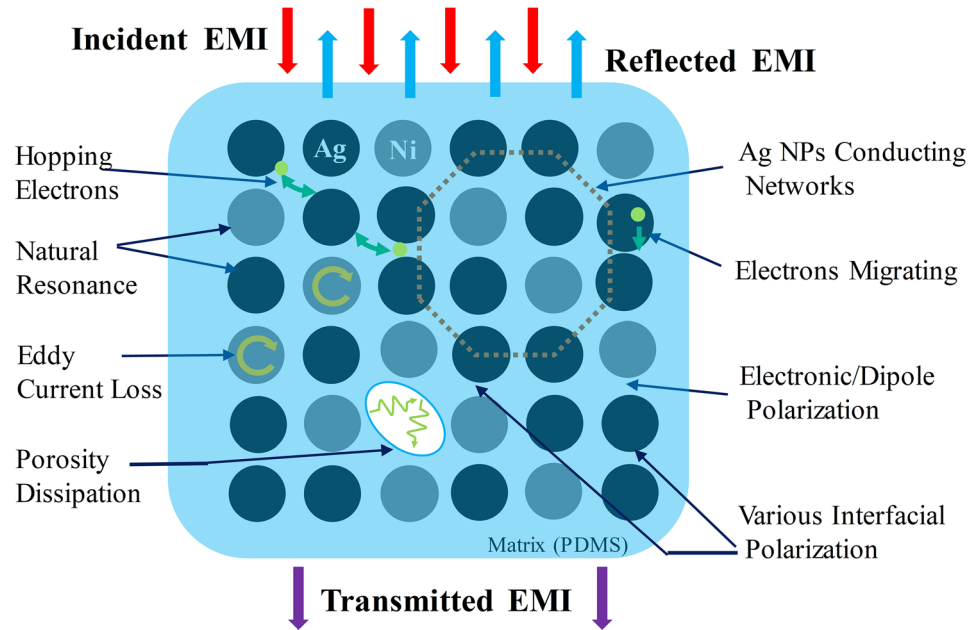

Figure 6 A summary of the stretchable and EMI shielding films.

**Figure 7** Schematic shows the shielding mechanism of FA.

eddy currents are generated. Dielectric properties of FA(Ni) at different frequency of EMI have proved the existence of polarization, as shown in Fig. 1e. In addition, due to the small size effect, the high surface energy of nanoparticles can lead to natural resonance. Nevertheless, the oxides in the Ni NPs have come together to form porosities, possibly carbon dioxide ones. Electromagnetic waves are reflected many times at gas–solid interface inside the porosity, then the wave crest and trough coincide, and the related energy dissipates in the form of heat energy. These factors also occurs in FA(Ag + Ni) and contributes much to the increase of the absorption, thus showing higher absorptivity.

To demonstrate the contribution of Ni NPs to the improvement of absorptivity, a layered structure is introduced into the preparation of the film. Taking into account the effect of thickness on absorption, the total thickness of the FA(Ag) and FA(Ni) layers on every film is still designed to be 0.7 mm. Experimental results show that the absorptivity of a two-layer film is greater than the reflectivity over the entire frequency range, which is completely different from that of a film with only one FA(Ag) layer. Moreover, by increasing the M(Ag) and M(Ni) in the two layers to optimize the current percolation, EMI SE is increased by 72.7–73.6%, and absorptivity in the high frequency range can reach an inflated 90.0%. Thus, the effect of Ni NPs in improving the absorptivity is evident. However, the EMI SE of the film

with this layered structure is much less than that of the pure FA(Ag) layer due to the deterioration of the overall conductivity of FA(Ni).

For the FA(Ag + Ni), the interfaces between Ag NPs and Ni NPs account for 8.82% of the total interface (as shown the EDS map in Fig. 2l). These heterogeneous media may lead to the interfacial polarization [9], which causes the loss of incident electrical and magnetic energy and the improvement of SE. Increasing the mass fraction of Ag NPs can contribute to the promotion of SE by more hopping and migrating electrons. It is necessary to find a balance point in the selection of M(Ag) and M(Ni), so as to ensure high absorption of electromagnetic interference, while simultaneously guaranteeing M(Ag) + M(Ni) < M_{lim} (Ag + Ni) in FA(Ag + Ni) to achieve stretchable properties. The total mass fraction, 47% < M(Ag) + M(Ni) < 50%, is thus identified. Next, FA with M(Ag) = 35%, M(Ni) = 14.8% and M(Ag) = 33%, and M(Ni) = 14.8% are studied. Before and after 20 000 cycles, sheet resistance of FA(Ag + Ni) is consistently larger than that of FA(Ag) due to the difference in conductivity. However, the small decrease in electrical conductivity for FA(Ag + Ni) does not affect the shielding effectiveness, unless there is further deterioration of the conductivity by reducing M(Ag) to 33%, compared to FA(Ag). In this situation, M(Ni) is 74.0% lower than in the film with double-layer structure, resulting in absorptivity that is still lower than the reflectivity. On

Figure 8 Illustration of a device that interferes with the transmission of electromagnetic signals. **a** Schematic of the tested circuit; **b** photograph of the brightness of the bulb with a shielding film; **c** photograph of the brightness of the bulb without a shielding film.
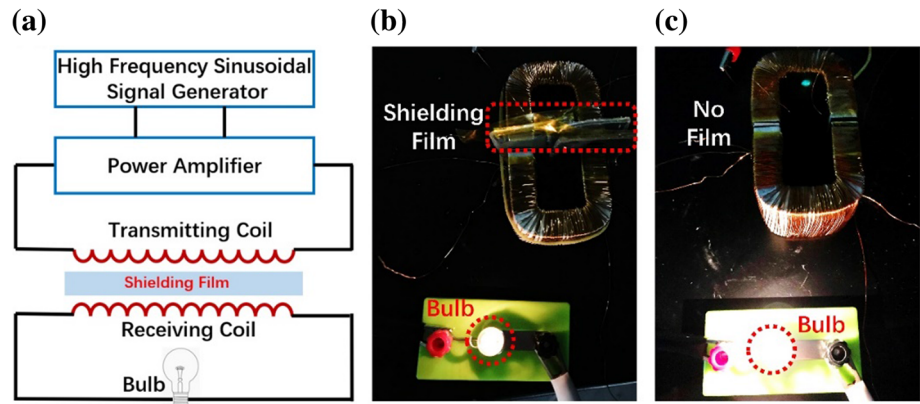
the other hand, the stretchable properties of FA are almost entirely contributed by PDMS. The M(PDMS) in FA(Ag + Ni) is 50–53%, slightly lower than that in FA(Ag) (57–60%), leading to a small reduction in maximum tensile strain remaining conductive.

A device that interferes with the transmission of EMI

A device which can change the output power of the transformer is also studied. The test circuit is shown in Fig. 8a. The transformer consists of double C-shaped iron cores, each wound with a copper coil of 200 turns. The power amplifier outputs a high-voltage signal to the transmitting coil after receiving a sinusoidal voltage generated by the signal generator. As the stretchable shielding film in this study interferes with the transmission of electromagnetic signals, the receiving coil can only output a low electrodynamic potential, resulting in low brightness of the bulb shown in Fig. 8b. After removing the shielding film, the bulb flashes a dazzling light, as seen in Fig. 8c.

Conclusion

A set of highly stretchable conductive and EMI shielding films were fabricated in this study. Various functional adhesives were composited using Ag NPs, Ni NPs, and liquid PDMS. The conductivity, permeability, and absorptivity of EMI, as well as stretchable properties, were determined by the content of Ag NPs, Ni NPs, and liquid PDMS. Compared to FA(Ag), FA(Ag + Ni) demonstrated superior EMI SE of up to 57.1 dB, and stretchable property of 225%. Reusability and prominent electrical properties were

tested under 20 000 stretching–releasing cycles of 0–100% and 0–150% strain. The contribution of the Ag NPs and magnetic Ni NPs to the absorptivity was also confirmed. Additionally, excellent durability was demonstrated by testing the electrical properties and EMI SE of such films after numerous days. A device to change the output power of a transformer to test the shielding film effect on the transmission of electromagnetic signals by the brightness of the bulb was then constructed. The excellent comprehensive performance of the proposed films demonstrates their wide application potential for communications electronics, medical, aerospace, wearable devices, and other areas.

Acknowledgements

Compliance with ethical standards

Conflicts of interest The authors declare that they have no competing interests.

References

[1] Yu YH, Ma CCM, Teng CC, Huang YL, Lee SH, Wang I, Wei MH (2012) Electrical, morphological, and electromagnetic interference shielding properties of silver nanowires and nanoparticles conductive composites. Mater Chem Phys 136:334–340

[2] Kim JJ, Lee HW, Dabhade VV, Kim SR, Kwon WT, Choi DJ, Kim H, Kim Y (2010) Electro magnetic interference shielding characteristic of silver coated copper powder. Met Mater Int 16:469–475

[3] Oh HJ, Dao VD, Choi HS (2018) Electromagnetic shielding effectiveness of a thin silver layer deposited onto PET film via atmospheric pressure plasma reduction. Appl Surf Sci 435:7–15

[4] Ma J, Wang K, Zhan M (2015) A comparative study of structure and electromagnetic interference shielding performance for silver nanostructure hybrid polyimide foams. RSC Adv 5:65283–65296

[5] Ma X, Zhang Q, Chen X, Wu G (2014) Geomagnetic shielding property and mechanism of Fe–Ni laminated composite. Acta Metall Sin 27:918–923

[6] Gao Y, Huang L, Zheng ZJ, Li H, Zhu M (2007) The influence of cobalt on the corrosion resistance and electromagnetic shielding of electroless Ni–Co–P deposits on Al substrate. Appl Surf Sci 253:9470–9475

[7] Ajitha AR, Arif MP, Aswathi MK, Mathew LP, Geethamma VG, Kalarikkal N (2018) An effective EMI shielding material based on poly(trimethylene terephthalate) blend nanocomposites with multiwalled carbon nanotubes. New J Chem 42:13915–13926

[8] Wang R, He F, Wan Y, Qi Y (2012) Preparation and characterization of a kind of magnetic carbon fibers used as electromagnetic shielding materials. J Alloys Compd 514:35–39

[9] Singh BP, Saket DK, Singh AP, Pati S, Gupta TK, Singh VN, Dhakate SR, Dhawan SK, Kotnala RK, Mathur RB (2015) Microwave shielding properties of Co/Ni attached to single walled carbon nanotubes. J Mater Chem A 3:13203–13209

[10] Shen B, Zhai W, Zheng W (2014) Ultrathin flexible graphene film: an excellent thermal conducting material with efficient EMI shielding. Adv Funct Mater 24:4542–4548

[11] Hsiao ST, Ma CC, Liao WH, Wang YS, Li SM, Huang YC, Yang RB, Liang WF (2014) Lightweight and flexible reduced graphene oxide/water-borne polyurethane composites with high electrical conductivity and excellent electromagnetic interference shielding performance. ACS Appl Mater Interfaces 6:10667–10678

[12] Hu M, Gao J, Dong Y, Li K, Shan G, Yang S, Li RK (2012) Flexible transparent PES/silver nanowires/PET sandwich-structured film for high-efficiency electromagnetic interference shielding. Langmuir 28:7101–7106

[13] Kumar A, Singh AP, Kumari S, Srivastava AK, Bathula S, Dhawan SK, Dutta PK, Dhar A (2015) EM shielding effectiveness of Pd–CNT–Cu nanocomposite buckypaper. J Mater Chem A 3:13986–13993

[14] Rengasamy K, Sakthivel DK, Natesan B, Muthukaruppan A, Venkatachalam S, Kannaiyan D (2016) Enhanced electromagnetic interference shielding in a Au–MWCNT composite nanostructure dispersed PVDF thin films. J Phys Chem C 120:13771–13778

[15] Shi Y-D, Li J, Tan Y-J, Chen Y-F, Wang M (2019) Percolation behavior of electromagnetic interference shielding in polymer/multi-walled carbon nanotube nanocomposites. Compos Sci Technol 170:70–76

[16] Liu Y, Lu M, Wu K, Yao S, Du X, Chen G, Zhang Q, Liang L, Lu M (2019) Anisotropic thermal conductivity and electromagnetic interference shielding of epoxy nanocomposites based on magnetic driving reduced graphene oxide@Fe$_3$O$_4$. Compos Sci Technol 174:1–10

[17] Liu Y, Zhang K, Mo Y, Zhu L, Yu B, Chen F et al (2018) Hydrated aramid nanofiber network enhanced flexible expanded graphite films towards high EMI shielding and thermal properties. Compos Sci Technol 168:28–37

[18] Liu J, Zhang HB, Sun R, Liu Y, Liu Z, Zhou A, Yu ZZ (2017) Hydrophobic, flexible, and lightweight MXene foams for high-performance electromagnetic-interference shielding. Adv Mater 29:1702367. https://doi.org/10.1002/adma.201702367

[19] Lee SH, Kang D, Oh IK (2017) Multilayered graphene-carbon nanotube-iron oxide three-dimensional heterostructure for flexible electromagnetic interference shielding film. Carbon 111:248–257

[20] Zhen X, Zheng L, Haiyan S, Chao G (2013) Highly electrically conductive Ag-doped graphene fibers as stretchable conductors. Adv Mater 25:3249–3253

[21] Catenacci MJ, Reyes C, Cruz MA, Wiley BJ (2018) Stretchable conductive composites from Cu–Ag nanowire felt. ACS Nano 12:3689–3698

[22] Ryu S, Lee P, Chou JB, Xu R, Zhao R, Hart AJ, Kim SG (2015) Extremely elastic wearable carbon nanotube fiber strain sensor for monitoring of human motion. ACS Nano 9:5929–5936

[23] Xu M, Qi J, Li F, Zhang Y (2018) Highly stretchable strain sensors with reduced graphene oxide sensing liquids for wearable electronics. Nanoscale 10:5264–5271

[24] Lee MS, Lee K, Kim SY, Lee H, Park J, Choi KH, Kim HK, Kim DG, Lee DY, Nam S, Park JU (2013) High-performance, transparent, and stretchable electrodes using

graphene-metal nanowire hybrid structures. Nano Lett 13:2814–2821

[25] Yang S, Liu P, Yang M, Wang Q, Song J, Dong L (2016) From flexible and stretchable meta-atom to metamaterial: a wearable microwave meta-skin with tunable frequency selective and cloaking effects. Sci Rep 6:21921. https://doi.org/10.1038/srep21921

[26] Kato Y, Horibe M, Ata S, Yamada T, Hata K (2017) Stretchable electromagnetic-interference shielding materials made of a long single-walled carbon nanotube-elastomer composite. RSC Adv 7:10841–10847

[27] Chen M, Zhang L, Duan S, Jing S, Jiang H, Luo M, Li C (2014) Highly conductive and flexible polymer composites with improved mechanical and electromagnetic interference shielding performances. Nanoscale 6:3796–3803

[28] Kim E, Lim DY, Kang Y, Yoo E (2016) Fabrication of a stretchable electromagnetic interference shielding silver nanoparticle/elastomeric polymer composite. RSC Adv 6:52250–52254

[29] Jung J, Lee H, Ha I, Cho H, Kim KK, Kwon J, Won P, Hong S, Ko SH (2017) Highly stretchable and transparent electromagnetic interference shielding film based on silver nanowire percolation network for wearable electronics applications. ACS Appl Mater Interfaces 9:44609–44616

[30] Li P, Du D, Guo L, Guo Y, Ouyang J (2016) Stretchable and conductive polymer films for high-performance electromagnetic interference shielding. J Mater Chem C 4:6525–6532

[31] Zhang Q, Liang Q, Zhang Z, Kang Z, Liao Q, Ding Y, Ma M, Gao F, Zhao X, Zhang Y (2017) Electromagnetic shielding hybrid nanogenerator for health monitoring and protection. Adv Funct Mater 28:1703801. https://doi.org/10.1002/adfm.201703801

[32] Joseph N, Janardhanan C, Sebastian MT (2014) Electromagnetic interference shielding properties of butyl rubber-single walled carbon nanotube composites. Compos Sci Technol 101:139–144

[33] Jia LC, Zhang G et al (2019) Robustly superhydrophobic conductive textile for efficient electromagnetic interference shielding. ACS Appl Mater Interfaces 11:1680–1688

[34] Jia LC, Yan DX et al (2017) High strain tolerant EMI shielding using carbon nanotube network stabilized rubber composite. Adv Mater Technol 2:1700078. https://doi.org/10.1002/admt.201700078

[35] Shahzad F, Alhabeb M et al (2016) Electromagnetic interference shielding with 2D transition metal carbides (MXenes). Science 353(6304):1137–1140

[36] Lee SH, Yu S et al (2017) Density-tunable lightweight polymer composites with dual-functional ability of efficient EMI shielding and heat dissipation. Nanoscale 9:13432–13440

[37] Li W, Xiong L, Pu Y, Quan Y, Li S (2019) High-performance paper-based capacitive flexible pressure sensor and its application in human-related measurement. Nanoscale Res Lett 14:183. https://doi.org/10.1186/s11671-019-3014-y

[38] Zhang T, Wang F, Zhang P, Wang Y, Chen H, Li J et al (2019) Low-temperature processed inorganic perovskites for flexible detectors with a broadband photoresponse. Nanoscale 11(6):2871–2877

[39] Gu Y, Zhang T, Chen H, Wang F, Pu Y, Gao C et al (2019) Mini review on flexible and wearable electronics for monitoring human health information. Nanoscale Res Lett 14:263. https://doi.org/10.1186/s11671-019-3084-x

[40] Feng P, Ji H et al (2019) Highly stretchable patternable conductive circuits and wearable strain sensors based on polydimethylsiloxane and silver nanoparticles. Nanotechnology 30:185501. https://doi.org/10.1088/1361-6528/ab013b

[41] Park M, Park J, Jeong U (2014) Design of conductive composite elastomers for stretchable electronics. Nano Today 9:244–260